THE JOURNAL OF BIOLOGICAL CHEMISTRY VOL. 289, NO. 27, pp. 18860–18872, July 4, 2014

Structural Determinants of Phosphatidylinositol 4,5-Bisphosphate (PIP_2) Regulation of BK Channel Activity through the RCK1 Ca^{2+} Coordination Site[*]

Received for publication, December 1, 2013, and in revised form, April 22, 2014 Published, JBC Papers in Press, April 28, 2014, DOI 10.1074/jbc.M113.538033

Qiong-Yao Tang[‡§¶1], Zhe Zhang[‡§¶], Xuan-Yu Meng[‡], Meng Cui[‡], and Diomedes E. Logothetis[‡2]

From the [‡]Department of Physiology and Biophysics, Virginia Commonwealth University School of Medicine, Richmond, Virginia 23298 and the [§]Jiangsu Province Key Laboratory of Anesthesiology and [¶]Jiangsu Province Key Laboratory of Anesthesia and Analgesia Application Technology, Xuzhou Medical College, Xuzhou 221004, China

Background: PIP_2 has been reported to enhance Ca^{2+}-driven gating, but the molecular determinants of this interplay are not known.
Results: PIP_2 interacts with specific basic residues and enhances Ca^{2+} gating through the αA-KDRDD-αB structural elements.
Conclusion: The RCK1 Ca^{2+}-binding site is coupled to PIP_2.
Significance: PIP_2 is a key element in the regulation of BK channel activity.

Big or high conductance potassium (BK) channels are activated by voltage and intracellular calcium (Ca^{2+}). Phosphatidylinositol 4,5-bisphosphate (PIP_2), a ubiquitous modulator of ion channel activity, has been reported to enhance Ca^{2+}-driven gating of BK channels, but a molecular understanding of this interplay or even of the PIP_2 regulation of this channel's activity remains elusive. Here, we identify structural determinants in the KDRDD loop (which follows the αA helix in the RCK1 domain) to be responsible for the coupling between Ca^{2+} and PIP_2 in regulating BK channel activity. In the absence of Ca^{2+}, RCK1 structural elements limit channel activation through a decrease in the channel's PIP_2 apparent affinity. This inhibitory influence of BK channel activation can be relieved by mutation of residues that (*a*) connect either the RCK1 Ca^{2+} coordination site (Asp^{367} or its flanking basic residues in the KDRDD loop) to the PIP_2-interacting residues (Lys^{392} and Arg^{393}) found in the αB helix or (*b*) are involved in hydrophobic interactions between the αA and αB helix of the RCK1 domain. In the presence of Ca^{2+}, the RCK1-inhibitory influence of channel-PIP_2 interactions and channel activity is relieved by Ca^{2+} engaging Asp^{367}. Our results demonstrate that, along with Ca^{2+} and voltage, PIP_2 is a third factor critical to the integral control of BK channel activity.

The high conductance potassium (Maxi K, Big K, or BK) channel is activated by both membrane depolarization and increased intracellular Ca^{2+} concentrations ($[Ca^{2+}]_i$). Although Ca^{2+} and voltage are thought to act independently to regulate channel opening, a weak allosteric interaction between them makes the voltage sensor movement much more effective (1–4). The Slo1 pore-forming subunits of BK channels are composed of seven transmembrane segments (S0–S6) that assemble into tetramers. The S1–S4 transmembrane region of the Slo1α subunit forms a voltage-sensing domain, as in other voltage-gated channels, whereas the large C-terminal intracellular ligand-binding domain is responsible for sensing Ca^{2+} (5–13). Association of the Slo1α subunit with tissue-specific two-transmembrane β1–β4 subunits modifies its functional characteristics (14). The BK channel is expressed in a wide variety of tissues, most notably in the brain and smooth muscle-containing organs, but also among other tissues in reproductive organs (ovary, testes), in the pancreas, and in adrenal glands (15). In humans, malfunction of the BK channel is known to be important to the pathophysiology of epilepsy (16–19), hypertension (20–24), cancer (25–28), and asthma (29).

The Slo1 cytosolic domain is composed of two RCK (regulator of K^+ conductance) domains, RCK1 and RCK2 (30). The first Ca^{2+}-binding site identified was in a region termed the Ca^{2+}-bowl that contains a series of Asp residues located in the RCK2 domain (6) (also see Fig. 1, *B*, *C* (*left*), and *D* (*bottom*)). The second Ca^{2+}-binding site was identified in the RCK1 domain at position Asp^{367} (Fig. 1, *A* and *D* (*top*), shows Asp^{367} in the KDRDD loop in *yellow*) (10). Subsequently, the side chain of Glu^{535} (Fig. 1*C*, *right*) was reported to be a part of the RCK1 Ca^{2+} coordination site together with Asp^{367} (31). High-resolution crystal structures of the cytosolic domain have been obtained either with the RCK2 Ca^{2+}-bowl occupied by Ca^{2+} (PDB[3] code 3MT5) (32) or in the absence of Ca^{2+} (PDB code 3NAF) (33). Ca^{2+} has not yet been resolved in the RCK1 site, although the side chains of Asp^{367} and Glu^{535} are positioned such that they could coordinate Ca^{2+} (Fig. 1*C*, *right*, 3NAF structure). Interestingly, in the presence of Ca^{2+} in the Ca^{2+}-bowl, Asp^{367} and Glu^{535} point away from each other,

---

[*] This work was supported, in whole or in part, by National Institutes of Health (NIH) Grants R01-HL059949 and R01-HL090882 (to D. E. L.) and by NIH, NCRR, Grant S10RR027411 (to M. C.). This work was also supported by American Heart Association Grant 09SDG2290002 (to Z. Z.).

[1] To whom correspondence may be addressed: Dept. of Physiology and Biophysics, Virginia Commonwealth University School of Medicine, Richmond, VA 23298. Tel.: 804-828-5878; Fax: 804-828-7382; E-mail: qtang@vcu.edu.

[2] To whom correspondence may be addressed: Dept. of Physiology and Biophysics, Virginia Commonwealth University School of Medicine, Richmond, VA 23298. Tel.: 804-828-5878; Fax: 804-828-7382; E-mail: delogothetis@vcu.edu.

[3] The abbreviations used are: PDB, Protein Data Bank; PIP_2, phosphatidylinositol 4,5-bisphosphate; 5D5N, D897N/D901N; Wtmn, wortmannin; G-V, conductance-voltage; Ab, antibody; poly-K^+, polylysine.

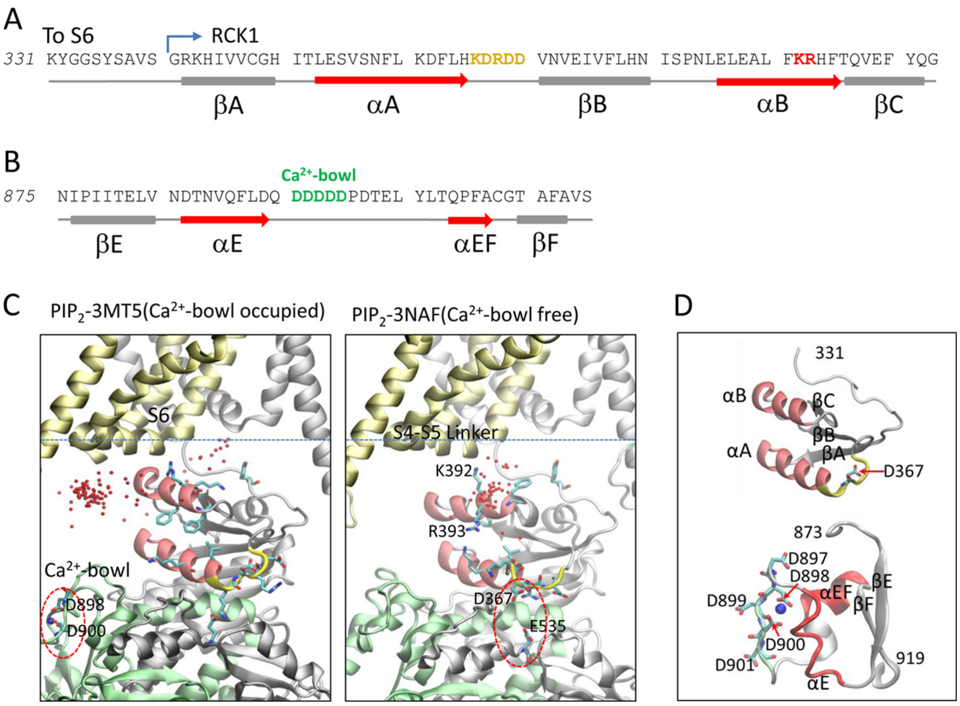

FIGURE 1. **RCK structural elements involved in Ca^{2+} sensing in Slo1 channels; relation to PIP_2 revealed by docking.** *A*, sequence with secondary structure elements of the mouse Slo1α channel following the S6 inner helix and through the βC strand of the RCK1 domain. The KDRDD loop (Lys^{366}–Asp^{370}) is *highlighted* in *yellow*, and the Lys^{392}/Arg^{393} residues, which communicated directly with PIP_2, are shown in *red*. *B*, sequence with secondary structure elements containing the Ca^{2+}-bowl in the RCK2 domain. The Ca^{2+}-bowl (Asp^{897}–Asp^{901}) is shown in *green*. *C*, structural models of Slo1 incorporating crystal structures of cytosolic domains in the presence and absence of Ca^{2+}. *Left*, *ribbon structures* of two subunits of the mSlo1α subunit are shown, one in *gray* and the other in *gold*, whereas the RCK2 domain of the *gray* subunit has been *highlighted* in *green* (the other two subunits have been removed for clarity). This model was built based on the 3MT5 (cytosolic domain of Slo1 with the Ca^{2+}-bowl occupied (32)) and 2R9R (Kv1.2-Kv2.1 chimeric channel (56)) coordinates. PIP_2 headgroup (diC1) docking simulations were performed on this model, using Autodock. 100 docking runs were conducted to yield 100 conformations of diC1-channel complex. Each *red dot* represents the C1 atom of diC1, which indicates the location of diC1 in the complexes. Most PIP_2 headgroups were located nearest the S4-S5 linker, the RCK2 Ca^{2+}-bowl coordination site is *circled* (in *red*), and a Ca^{2+} ion is shown (in *blue*). *Right*, the same process as on the *left* but using the 3NAF coordinates (cytosolic domain of Slo1 in the absence of Ca^{2+} (33)). In this figure, all 100 positions of diC1 from the docking simulation result are shown (*red dots*). Most PIP_2 headgroups were located closest to the αB residues Lys^{392} and Arg^{393}. In addition, the binding energy from Autodock indicated that diC1 showed the most favorable binding energy in the 3NAF model. The putative RCK1 Ca^{2+} coordination site, showing the critical residues Asp^{367} and Glu^{535} pointing toward each other, is *circled* (in *red*). *D*, the RCK1 structural elements that harbor the KDRDD loop containing Asp^{367} with its two neighboring basic residues (*top*) and the RCK2 structural elements that comprise the Ca^{2+}-bowl with five critical Asp residues directly coordinate the Ca^{2+} ion (*bottom*).

such that they could not possibly coordinate Ca^{2+} (Fig. 1*C*, *left*, 3MT5 structure). Despite these structural advances in the Ca^{2+}-sensing cytosolic domains, the lack of a full-length structure that includes the transmembrane domains as well as the lack of the RCK1 Ca^{2+}-bound state have precluded a structural understanding of how the channel is gated by either voltage or Ca^{2+} and how the weak allosteric coupling between these two gating mechanisms greatly enhances channel activation.

Phosphatidylinositol 4,5-bisphosphate (PIP_2), which has been shown to activate most ion channels and transporters (34, 35), has also been reported to directly activate BK channels by a single study (36). PIP_2 was found to enhance Ca^{2+}-driven gating by increasing mean open time and decreasing mean closed time kinetics. The PIP_2-induced activation was also found to be potentiated by the β1 but not by the β4 accessory channel subunits. These PIP_2 effects were found to be relevant in vascular myocytes, possibly contributing to the BK control of vascular tone.

We set out to investigate the structural determinants of the Ca^{2+}-dependent PIP_2 regulation of Slo1α activity. We expressed the mSlo1α channel in *Xenopus* oocytes and mainly used inside-out macropatches to study regulation of its activity by PIP_2. Increases in $[Ca^{2+}]_i$ enhanced the apparent affinity for PIP_2 through the Ca^{2+} coordination residue Asp^{367} in the KDRDD loop. Furthermore, in the absence of $[Ca^{2+}]_i$, it became clear that Asp^{367} as well as its two flanking basic residues, Lys^{366} and Arg^{368} (Fig. 1*A*), served to inhibit channel activation by decreasing the apparent affinity for PIP_2. These results suggested that the KDRDD loop exerted an inhibitory effect on channel activation through PIP_2. Mutagenesis results showed that this coupling proceeded from the KDRDD loop through the αA helix to the αB helix (Fig. 1*D*, *top*). PIP_2 docking simulations with the two available crystal structures and mutagenesis identified two basic residues in the αB helix, Lys^{392} and Arg^{393}, as critical elements in the coordination of PIP_2 (Fig. 1*C*, *right*). These results suggest that PIP_2 could serve in the role of allosterically coupling the cytosolic RCK1 structural elements (KDRDD loop, αA and αB helices) to the membrane-gating elements of the channel.

EXPERIMENTAL PROCEDURES

Mutagenesis and Channel Expression—Mouse Slo1 (mSlo1) cDNA was a gift from the laboratory of Dr. Christopher Lingle (Washington University, St. Louis, MO), of which the vector pXMX was designed to promote expression or increase RNA stability (10, 37–39). All mutations were generated by *Pfu*-

based mutagenesis using the QuikChange™ kit and verified by sequencing. cRNA was transcribed using the MessageMachine kit SP6 (Ambion) and injected into *Xenopus laevis* oocytes (0.3–5 ng/oocyte), depending on the expression level of the given channel protein. *X. laevis* oocytes were harvested and used for cRNA injection as described previously (40–42). Currents were normally recorded within ~2 weeks.

Electrophysiology—Macroscopic currents were recorded from standard excised inside-out patches with an A-M 2400 patch clamp amplifier (A-M Systems, Inc.). pClamp (Molecular Devices) was used to drive stimulus protocols and digitize currents. The signals were low pass-filtered at 10 kHz and digitized at 20-μs intervals. The pipette solution contained 140 mM KMES (methanesulfonate), 20 mM KOH, 10 mM HEPES, 2 mM $MgCl_2$, pH 7.0. The composition of internal solution of 0 μM $[Ca^{2+}]_i$ to bathe the cytoplasmic face of patch membranes contained 140 mM KMES, 20 mM KOH, 10 mM HEPES, 5 mM EGTA, pH 7.0. The free $[Ca^{2+}]$ in nominal 0 μM $[Ca^{2+}]_i$ solution was presumably about 0.5 nM. To obtain the conductance-voltage (G-V) curves in different $[Ca^{2+}]_i$, currents were elicited by voltage pulses from −180 to 200 mV (20 ms) at 10-mV increments, whereas the voltages before and after the pulses were held at −120 mV. In 0 $[Ca^{2+}]_i$, currents were elicited by voltage pulses from −100 to 300 mV or to 380 mV for some mutants (8 ms) at 10-mV increments, unless otherwise mentioned, whereas the voltages before and after these pulses were held at −100 mV.

BK single-channel currents were recorded from oocytes under the standard inside-out patch configuration. The solutions in the pipette and bath were the same as used in macroscopic current recordings except that 2 mM $MgCl_2$ and$[Ca^{2+}]_i$ concentrations were changed as indicated. Activity rundown in different intracellular $[Ca^{2+}]_i$ was measured 20–30 min following excision at the indicated voltage. 10 μM PIP_2 was perfused from the intracellular side (bath solution), and its effect was measured 5 min later when the BK channel activity reached steady state. Preparation of different $[Ca^{2+}]$ solutions was as described previously (37, 43).

Whole-cell currents in *Xenopus* oocytes were recorded by conventional two-electrode voltage clamp as described previously (40). Recordings were performed with a GeneClamp500 amplifier (Axon Instruments) 3–5 days after cRNA injection. Electrodes were filled with 1.5% (w/v) agarose in 3 M KCl. The bath was perfused with the same solution as that used in the pipette solution for inside-out patches. Microelectrodes had a resistance of 0.3–1.0 megaohms.

Wortmannin (Wtmn) treatment involved incubation of oocytes for 2–2.5 h before recording. In experiments with intact oocytes, intracellular Ca^{2+} levels were controlled by application of 2 nM ionomycin in the bath that contained different Ca^{2+} concentrations. Data acquisition and analysis were carried out using pClamp9 (Molecular Devices) and Origin (Microcal) software.

Data Analysis—The relative conductance was determined by measuring the steady-state current amplitudes at the indicated voltages. The G-V curves were fitted with the Boltzmann function,

$$\frac{G}{G_{\max}} = \frac{1}{1 + \exp\left(-\frac{ze(V - V_{1/2})}{kT}\right)} \qquad \text{(Eq. 1)}$$

where $G/G_{\max}$ is the ratio of conductance to maximal conductance, z is the number of equivalent charges, e is the elementary charge, V is membrane potential, and $V_{1/2}$ is the voltage where $G/G_{\max}$ reaches half of the maximum. k is Boltzmann's constant, and T is the absolute temperature.

Data in all figures are expressed as mean ± S.E. Statistical significance was evaluated by Student's t test, and $p < 0.05$ was considered significant.

Homology Modeling—The crystal structures of Kv1.2/2.1 (PDB code 2R9R), hSlo1 (PDB code 3MT5 for the Ca^{2+}-bowl-occupied model, and 3NAF for the Ca^{2+}-bowl-free model) were used as templates to develop homology models for the mSlo1 channel. In order to build the homology model of mSlo1, we first constructed a hybrid model template composed of the Kv1.2/Kv2.1 structure and of the hSlo1 3NAF structure. The structure of the Kv1.2/Kv2.1 S1–S6 was docked onto the hSlo1 structure based on the orientation of the four BK linkers. We then used the fused crystal structure templates (Kv1.2/2.1 transmembrane domains) and mSlo1 channel (GI: 347144) for sequence alignment using the ClustalW server (44), followed by minor manual adjustments in non-homologous regions.

We also built an mSlo1 model based on the 3MT5 crystal structure of hSlo1. Because 3MT5 was crystallized as a monomer and did not contain the BK linker, we used the 2R9R-3NAF structure to construct the hybrid template of 2R9R-3MT5. The 3MT5-based homology model of mSlo1 was then built based on the hybrid template of 2R9R-3MT5. Homology models of the mSlo1 channel were generated using the MODELLER program (45).

PIP_2 and Slo1 Docking—We used the AUTODOCK program (46) to dock the PIP_2 headgroup into the mSlo1 model structures. The grid-based potential maps that were generated for the mSlo1 channel, using CHNOP (*i.e.* carbon, hydrogen, nitrogen, oxygen, and phosphorus) elements, sampled on a uniform grid containing 100 × 70 × 100 points, were 0.375 Å apart for the free energy calculations. The grid box was centered at the side chain of residue Arg^{393} of mSlo1, which was found by our functional studies to be important for PIP_2 sensitivity. The Lamarckian genetic algorithm was used to identify the docking conformations of the PIP_2 headgroup. 100 docking simulations were performed. The final docked PIP_2 headgroup configurations were selected based on docked binding energies and cluster analysis. Two potential binding sites of mSlo1 channel for PIP_2 were identified by docking simulations, formed by positively charged residues Lys^{392} and Arg^{393}.

Chemicals—diC8 PIP_2 and PIP_2 antibody (PIP_2 Ab) were purchased from Avanti Polar Lipids. Other chemicals, such as Wtmn, ionomycin, Mg-ATP, and polylysine (poly-K^+) were purchased from Sigma-Aldrich. Stocks and working solutions were prepared using protocols according to the manufacturer's instructions.

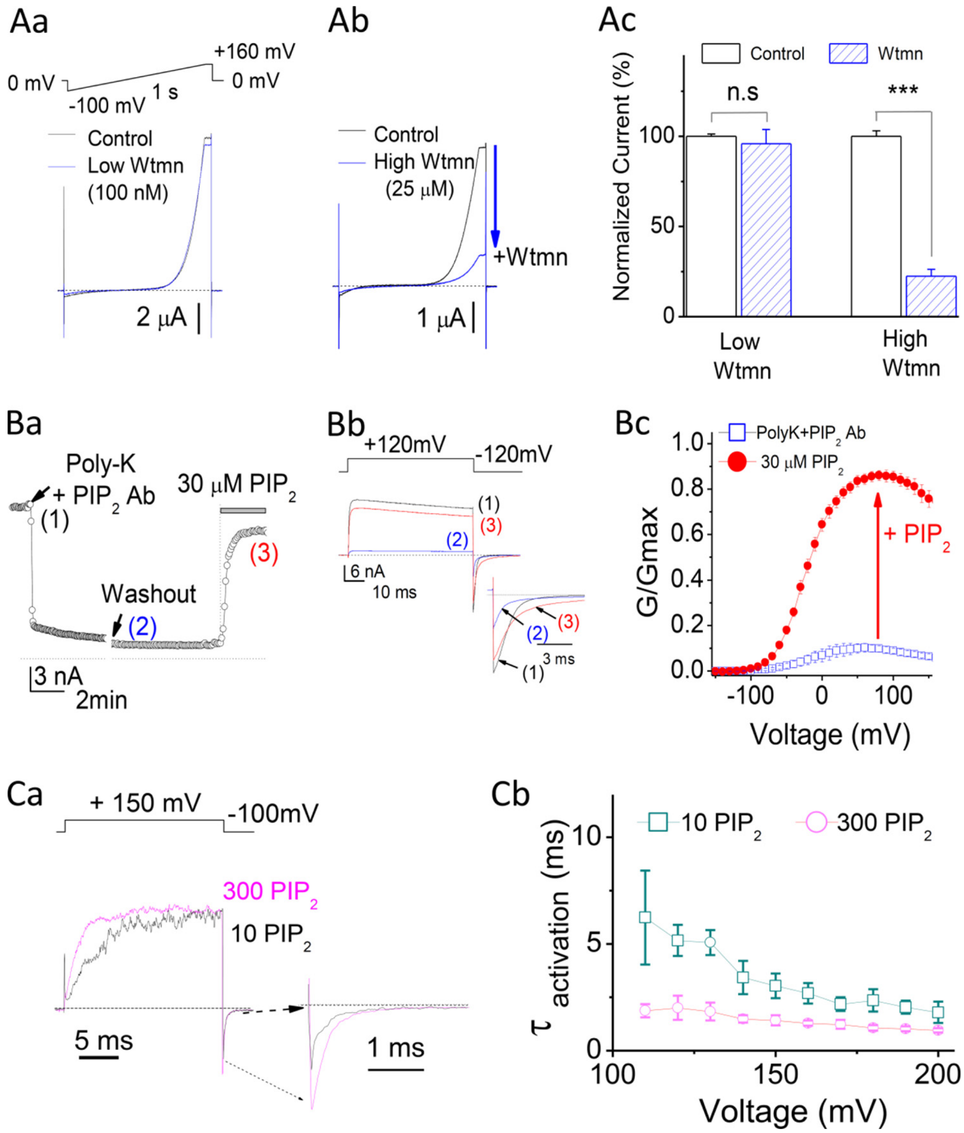

FIGURE 2. **Slo1 channels are sensitive to PIP_2.** *Aa*, effect of a 2-h preincubation with 100 nM Wtmn on Slo1 currents. Current traces were evoked by a voltage ramp protocol (*top*) ranging from −100 to +160 mV (1 s), using whole-cell (two-electrode voltage clamp) recordings in oocytes. *Ab*, same as in *Aa* but preincubated with 25 μM Wtmn. *Ac*, summary bar graphs from *Aa* and *Ab*. *Ba*, time course recording of Slo1 current amplitude of an inside-out macropatch recording from *Xenopus* oocytes injected with mSlo1 channels. Slo1 current in 100 μM $[Ca^{2+}]_i$ was inhibited by PIP_2 scavengers PIP_2 Ab (1–2:1000) + poly-K^+ (300 μg/ml) but was reactivated by exogenous application of 30 μM PIP_2. *Bb*, representative traces for Slo1 currents recorded at the time points indicated by *numbers* (*1–3*, *color-coded*) in *Ba*. Current traces were evoked by the voltage step protocol shown above. *Inset*, tail currents expanded. *Bc*, normalized G-V curves for Slo1 in 30 μM $[Ca^{2+}]_i$ showing the reactivation of Slo1 channels by PIP_2 following current inhibition by PIP_2 Ab (1–2:1000) + 300 μg/ml poly-K^+. *Ca*, the actual macroscopic current traces were recorded in the presence of 10 μM (*black*) or 300 μM PIP_2 (*purple*). Voltage was stepped from a holding potential of −100 mV to +150 mV and then back to −100 mV. The current trace in 10 μM PIP_2 was rescaled to have the same peak amplitude with that in 300 μM PIP_2 (*purple*). *Inset*, tail currents expanded. $[Ca^{2+}]_i = 0$ μM. *Cb*, activation time constants by 10 μM (□) or 100 μM (○) PIP_2 following depletion of endogenous PIP_2 by PIP_2 scavengers (*PIP_2 Ab* (1–2:1000) + poly-K^+ (300 μg/ml). *Error bars* indicate mean ± S.E.

RESULTS

Slo1 Channels Are PIP_2-sensitive—Consistent with the conclusions of Vaithianathan *et al.* (36), we also found that Slo1 channels expressed in *Xenopus* oocytes are PIP_2-sensitive. Scavenging of endogenous PIP_2 with a combination of poly-K^+ and PIP_2 Ab in excised patches or treatment with micromolar concentrations of Wtmn in intact cells caused significant inhibition of Slo1 currents (Fig. 2*A*). Wtmn is known to block the activity of most phosphatidylinositol 3-kinases at nanomolar concentrations. 100 nM Wtmn showed no effect on BK currents (Fig. 2, *Aa* and *Ac*). In contrast, 25 μM wortmannin, which also blocks phosphatidylinositol 4-kinases, thus reducing resynthesis of PIP_2 to the plasma membrane, showed strong inhibition of BK currents (Fig. 2, *Ab* and *Ac*). Moreover, direct application of PIP_2, in excised patches that had been previously treated with a combination of polylysine and PIP_2 antibody to deplete endogenous PIP_2, showed robust current reactivation (Fig. 2*B*). PIP_2 altered the voltage-dependent activation kinetics of Slo1 currents. 300 μM PIP_2 showed faster activation kinetics than 10 μM PIP_2, especially at depolarizations to less positive potentials (Fig. 2, *Ca* and *Cb*).

Rundown of Slo1 Unitary Currents and Reactivation by PIP_2—Single channel recordings in the inside-out mode of the patch clamp technique held at +40 mV in $[Ca]_i$ = 100 μM

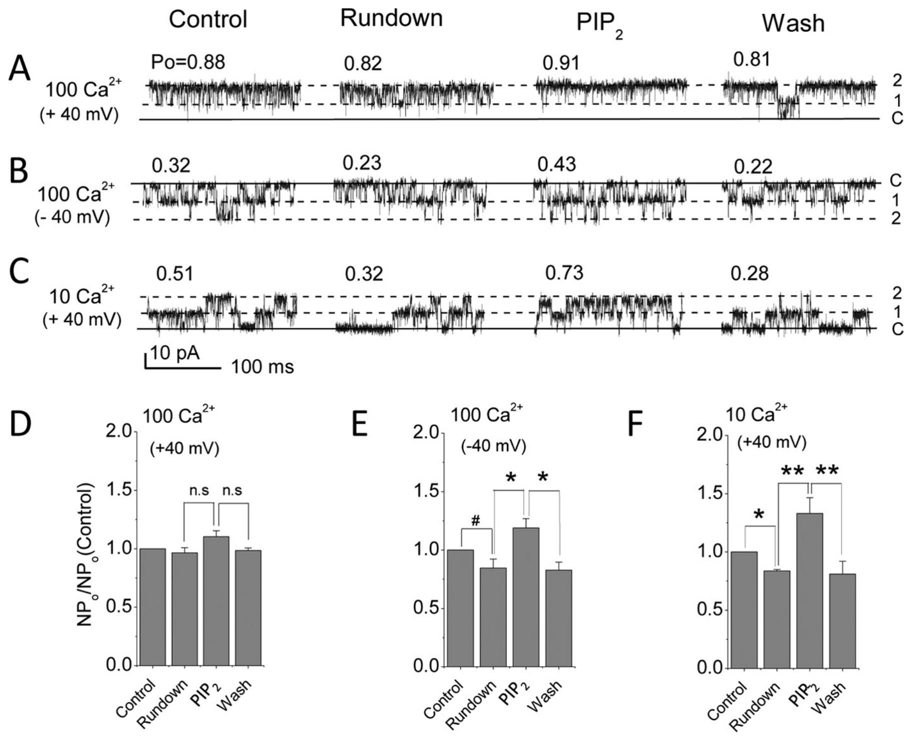

FIGURE 3. **Rundown of unitary activity and PIP_2 reactivation.** *A*, unitary currents obtained upon excision (*Control*), rundown (>20 min following inside-out patch excision), PIP_2 (5 min later after channel activation reached steady state), and washout in 100 μM Ca^{2+}. *Solid line*, channel closed level (*labeled* as *C*); *1* and *2*, number of open channel current levels. P_o for each current is indicated *above* the *trace*. $V = +40$ mV. *B*, same as in *A* but held at -40 mV. *C*, same as in *A*, but in 10 μM Ca^{2+}. *D*, averaged NP_o responses to rundown, PIP_2, and washout at $+40$ mV in 100 Ca^{2+}. *E*, same as in *D* but at -40 mV; *F*, same as in *D* but in 10 μM Ca^{2+} ($n = 3$–6). #, $p < 0.05$; *, $p < 0.01$; **, $p < 0.005$. *Error bars* indicate mean ± S.E.

showed high open probability ($P_o = 0.88$; Fig. 3, *A* and *D*) immediately after excision. Under these conditions, no significant rundown of activity was seen, and 10 μM PIP_2 did not enhance further channel activity. In contrast, if the patch was held at -40 mV, activity showed significant rundown, and diC8-PIP_2 stimulated activity significantly in a reversible manner (Fig. 3, *B* and *E*). This enhanced sensitivity to PIP_2 of channel activity in more depolarized membranes has been described for other channels (*e.g.* TRPM8 (47)). In 10 μM $[Ca^{2+}]_i$ concentrations, rundown and reversible reactivation by PIP_2 were highly significant (Fig. 3, *C* and *F*). At 1 μM $[Ca^{2+}]_i$, we observed even stronger rundown both at $+40$ and $+80$ mV (data not shown). Interestingly, 10 μM diC8-PIP_2 was not enough to reactivate this channel at either $+40$ or $+80$ mV, suggesting again a further decrease in PIP_2 sensitivity with a decrease in Ca^{2+} concentration. However, a higher diC8-PIP_2 concentration (40 μM) could partially reactivate BK channel activity at $+80$ mV (data not shown). Collectively, the experiments in Figs. 2 and 3 demonstrate the PIP_2 dependence of Slo1 current activation.

Ca^{2+} Binding to the Asp^{367} Site Enhances PIP_2 Affinity—We first compared the apparent affinity of the Slo1-WT channel to PIP_2 in solutions containing no added Ca^{2+} (assumed to be ~0.5 nM and referred to as 0 Ca^{2+}) and in the presence of 100 μM $[Ca^{2+}]_i$. In 0 Ca^{2+}, the $V_{1/2}$ of Slo1 was 173 mV ($n > 10$). In contrast, in 100 μM Ca^{2+}, the $V_{1/2}$ was shifted to ~ -7.8 mV ($n > 6$) (Fig. 4*A*). G-V relationships were constructed at different concentrations of diC8-PIP_2 after inhibition with poly-K^+ and PIP_2 Ab (just as shown in Fig. 2*B*), and the relative conductance values at $+170$ mV (for 0 Ca^{2+}) (Fig. 4*B*) or at -10 mV (for 100 μM Ca^{2+}) (Fig. 4*C*) were plotted as a function of the PIP_2 concentration tested (Fig. 4*D*). In the presence of 100 μM $[Ca^{2+}]_i$, the Slo1 channel's apparent affinity to PIP_2 increased ~2-fold relative to 0 μM $[Ca^{2+}]_i$ (Fig. 4, *B*–*D* and *G*). Similarly, in the presence of 100 μM $[Ca^{2+}]_i$, the apparent affinity to PIP_2 of an epilepsy-dyskinesia D369G mutant increased to a similar extent as the Slo1-WT compared with that in the absence of $[Ca^{2+}]_i$ (~3-fold; Fig. 4, *E* and *G*). D369G has been shown previously to increase channel activity by decreasing the flexibility of the KDRDD loop without influencing Ca^{2+} binding itself (48). Interestingly, compared with the wild type Slo1, the D369G mutant showed a significant enhancement in its PIP_2 apparent affinity both in the absence and in the presence of Ca^{2+} (Fig. 4*G*). Interestingly, the D367G mutant that disrupts the Ca^{2+} binding in the RCK1 domain also increased the apparent affinity for PIP_2 (Fig. 4, *F* and *G*). As expected, increasing $[Ca^{2+}]_i$ could not further enhance the PIP_2 affinity of the D367G mutant (Fig. 4, *F* and *G*) due to the absence of the local conformational change induced by Ca^{2+} binding. A similar result to the PIP_2 effect on the D367G mutant was obtained from the D367A mutant. (Fig. 5, *C* and *H*). To test whether neighboring residues to Asp^{367} affected the PIP_2 apparent affinity of the channel, additional mutants in the KDRDD loop were tested (Fig. 5, *A*–*H*). Results showed similar increases of PIP_2 affinity by the K366N and R368N but not by the D370N and D379N mutants (Fig. 5, *D*–*G*). These results suggested that the Asp^{367} residue that coordinates Ca^{2+} and its two flanking basic residues (Lys^{366} and Arg^{368}) are coupled to PIP_2 regulation of channel activity.

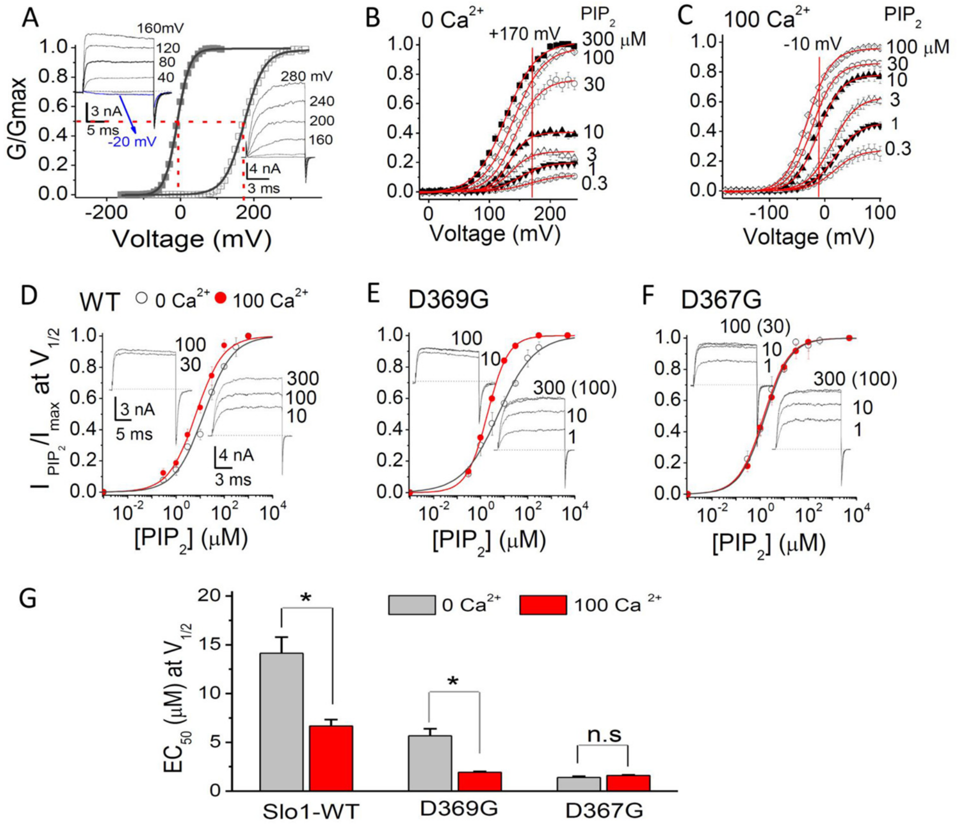

FIGURE 4. **The Ca^{2+} enhancement of the apparent PIP_2 affinity of Slo1 channels involves the RCK1 Ca^{2+} coordination site at Asp^{367}.** *A*, G-V curves of Slo1 WT channels in 0 (*open squares*) or 100 μM (*filled squares*) $[Ca^{2+}]_i$. *Solid lines*, fits to the Boltzmann function (see "Experimental Procedures"). $V_{1/2}$ is indicated by the *red dashed lines* ($V_{1/2} = +173$ mV in 0 μM $[Ca^{2+}]_i$ and -8 mV in 100 μM $[Ca^{2+}]_i$). Voltage protocols for G-V curves are described under "Experimental Procedures." Actual macroscopic current traces in 0 (*right*) and 100 μM $[Ca^{2+}]_i$ (*left*) are shown in the *insets*. For clarity, current traces shown are in 40-mV increments, as indicated. The voltages before and after the pulses were -120 mV in 100 μM $[Ca^{2+}]_i$ (*left*) and -100 mV in 0 μM $[Ca^{2+}]_i$ (*right*), respectively. *B*, G-V curves at 0 Ca^{2+} for WT Slo1 channels in different PIP_2 concentrations, as indicated. G-V curves at each PIP_2 concentration were obtained following endogenous PIP_2 depletion by PIP_2 scavengers (PIP_2 Ab (PIP_2 Ab (1–2:1000) + poly-K^+ (300 μg/ml)). The *solid lines* through the data points represent fits to a simple Boltzmann function. The *red vertical line* at +170 mV (near the $V_{1/2}$ determined in *A*) is used as a reference point to assess relative amplitude of PIP_2-elicited currents. Note that 300 μM PIP_2 induced further activation when compared with 100 μM PIP_2. *C*, same as in *B* but in 100 μM $[Ca^{2+}]_i$. The *red vertical line* at -10 mV (near the $V_{1/2}$ determined in *A*) is used as a reference point to assess the relative amplitude of PIP_2-elicited currents. Note that the conductance saturated at 100 μM $[Ca^{2+}]_i$. *D*, PIP_2 dose-response curves for Slo1 WT channels near $V_{1/2}$ at 170 mV in 0 $[Ca^{2+}]_i$ (*open symbols*) and at -10 mV in 100 μM $[Ca^{2+}]_i$ (*filled symbols*). The points in 0 Ca^{2+} were obtained from *B* (at 170 mV), and those at -10 mV at 100 μM Ca^{2+} are from *C*. *Solid lines* are fits to the Hill equation with an EC_{50} summarized in *G*. Note that the maximum values were obtained from fits to the Hill equation. Hill coefficients were 0.73 in 0 $[Ca^{2+}]_i$ and 0.76 in 100 μM $[Ca^{2+}]_i$. *E*, same as in *D* but for D369G. Hill coefficients were 0.57 in 0 $[Ca^{2+}]_i$ and 0.98 in 100 μM $[Ca^{2+}]_i$. *F*, same as in *D* but for D367G. Hill coefficients were 0.83 in 0 μM $[Ca^{2+}]_i$ and 0.83 in 100 μM $[Ca^{2+}]_i$. Macroscopic current traces (in *D–F*) in different concentrations of PIP_2 are shown on the *left* for 100 μM $[Ca^{2+}]_i$ and on the *right* for 0 $[Ca^{2+}]_i$. Currents were elicited by depolarization to +100 mV in 100 μM $[Ca^{2+}]_i$ (*left*) and by a step to +150 mV in 0 μM $[Ca^{2+}]_i$(*right*). The voltages before and after the pulses in 100 μM $[Ca^{2+}]_i$ were -120 mV and -100 mV in 0 μM $[Ca^{2+}]_i$, respectively. Note that at the same voltage (such as at 100 mV in 100 μM $[Ca^{2+}]_i$, as shown on the *left*, or 150 mV in 0 $[Ca^{2+}]_i$, as shown on the *right*), both mutations D369G and D367G dramatically enhanced channel PIP_2 apparent affinity. *G*, PIP_2 EC_{50} values determined from the Hill fits in 0 μM (*gray*) and 100 μM (*red*) $[Ca^{2+}]_i$ from *D–F*. *Error bars* indicate mean ± S.E. Data points represent 3–7 determinations. *, $p < 0.01$.

KDR Mutants of the KDRDD Loop Increase Slo1 Channel Activation in the Absence of Ca^{2+}—A hallmark of BK channel function is that intracellular Ca^{2+} binding can allosterically couple to the voltage sensor movement and enhance channel activity (1). In 300 μM Ca^{2+}, the $V_{1/2}$ of Slo1 shifted by as much as 190 mV (Fig. 6*A*) compared with 0 $[Ca^{2+}]_i$. As mentioned above, Ca^{2+} sensitivity in Slo1 channels is mainly conferred by two sites, the RCK2 Ca^{2+}-bowl (five consecutive Asp residues, 897–901 in mSlo1) and the RCK1 Asp^{367}/Glu^{535} Ca^{2+} coordination site (see Fig. *1*). Both Ca^{2+}-bowl 5D5N mutant (D897N/D901N) and Asp^{367}/Glu^{535} mutants significantly decreased the Ca^{2+}-induced shift in $V_{1/2}$ (Fig. 6, *B–D* and *I*). However, although the 5D5N (Fig. 6*B*) or Glu^{535} mutants (*e.g.* E535G or E535A) did not change the $V_{1/2}$ in the absence of Ca^{2+} (Fig. 6*C*), Asp^{367} mutants (*e.g.* D367G or D367A) induced significant leftward shifts of $V_{1/2}$ in the absence of Ca^{2+} (Fig. 6*D*). Mutation of the two basic residues flanking Asp^{367} (*i.e.* K366N and R368N; see Figs. 5*A* and 6, *top right*) caused similar left shifts of the $V_{1/2}$ in the absence of Ca^{2+}, without affecting the Ca^{2+}-induced shift in $V_{1/2}$ (Fig. 6, *E* and *F*). In contrast, mutants of the remaining two Asp residues of the KDRDD loop (D369N and D370N) did not show a significant effect (Fig. 6, *G* and *H*). Summarized data for $\Delta V_{1/2}$ compared with Slo1 WT in the presence of 300 and 0 μM Ca^{2+} are shown in Fig. 6, *I* and *J*. These results indicated that the KDR mutants of the KDRDD loop increased PIP_2 affinity (Fig. 5) and left-shifted activation of the channel in the absence of Ca^{2+} (Fig. 6, *D–F* and *J*), suggesting that these mutants increase Slo1 activity by increasing the channel's PIP_2 affinity.

Two Basic Residues in the αB Helix Involved in Direct Channel-PIP_2 Interactions—To gain insight into how PIP_2 interacts with Slo1, we performed 100 docking simulations of the PIP_2

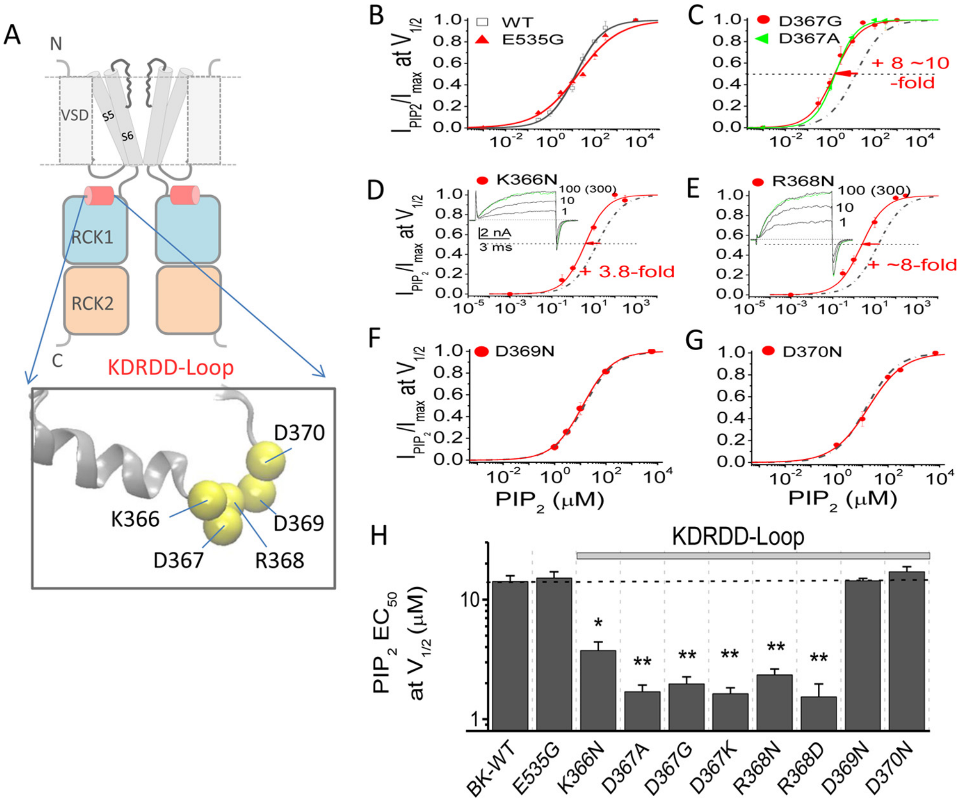

FIGURE 5. **Asp^{367} and its flanking basic residues decrease the apparent affinity of Slo1 channels for PIP_2.** *A*, *schematic* shows the KDRDD loop (Lys^{366}, Asp^{367}, Arg^{368}, Asp^{369}, and Asp^{370}) location in the RCK1 domain of two subunits of the tetrameric Slo1 channel. *B–G*, PIP_2 dose-response curves (constructed as in Fig. 4) of KDRDD and the Glu^{535} mutant channels in the absence of $[Ca^{2+}]_i$ compared with the WT (*dashed black curves*). Relative currents (I_{PIP2}/I_{max}) were obtained in response to PIP_2 application subsequent to the endogenous PIP_2 depletion (PIP_2 Ab (1–2:1000) + poly-K^+ (300 μg/ml) at a voltage near $V_{1/2}$ at 0 $[Ca^{2+}]_i$: 170 mV for E535G, 150 mV for D367G, 130 mV for D367A, 140 mV for K366N, 120 mV for R368N, 170 mV for D369N, and 180 mV for D370N). The $V_{1/2}$ in 0 $[Ca^{2+}]_i$ for each construct was as follows: 173.7 ± 1.9 mV for WT, 174.9 ± 1.2 for E535G, 145.5 ± 0.9 mV for D367G, 133.1 ± 0.8 mV for D367A, 140.2 ± 3.1 mV for K366N, 125.0 ± 2.2 mV for R368N, 167.2 ± 0.4mV for D369N, and 179 ± 2.9 mV for D370N ($n > 6–13$). Representative traces are shown for the two basic residues flanking Asp^{367}, namely K366N and R368N. The current traces shown in the *insets* at different PIP_2 concentrations were elicited from −100 to 120 mV and back to −100 mV. Note that the *overlapping traces* at 100 and 300 μM PIP_2; the *green current traces* are shown for the saturated activation levels reached at 100 μM PIP_2. *Solid curves*, fits to the Hill equation with the EC_{50} values summarized in *H*. Data points represent 3–5 determinations. *H*, EC_{50} at $V_{1/2}$ obtained by the Hill fits from *B–G*. *Dotted horizontal bar*, PIP_2 EC_{50} of the WT. *, $p < 0.01$; **, $p < 0.001$. *Error bars* indicate mean ± S.E.

headgroup (diC1) with either of two Slo1 models. These two models included a common homology model of the transmembrane domain of Slo1, using the Kv1.2/2.1 chimera (PDB code 2R9R) as a template together with each of the two available crystal structures of the cytosolic domains of this channel in the presence and absence of Ca^{2+} (PDB code 3MT5 and 3NAF, respectively). The C1 atom of the diC1 in each of the 100 conformations obtained is represented by *dots* in Fig. 1*C*. In the absence of Ca^{2+}, most of the diC1 molecules aggregated around the αB helix, involving the two basic residues, Lys^{392} and Arg^{393} (Figs. 1*C* (*right*) and 7*A*), in marked contrast to the docking simulations in the presence of Ca^{2+} bound to the Ca^{2+}-bowl (Fig. 1*C*, *left*). Next, we tested experimentally whether these two residues are involved in PIP_2 sensitivity. First, electrophysiological data showed that although both K392N and R393N mutants inhibited activation of Slo1 in the absence of Ca^{2+} (Fig. 7, *B*, *C*, and *E*), only the R393N mutant showed a parallel shift of $V_{1/2}$ in the presence of Ca^{2+} (Fig. 7, *C and E*). Furthermore, both neutralization mutations of Lys^{392} and Arg^{393} right-shifted the diC8-PIP_2 dose-response relationships, causing a 5–6-fold increase in the PIP_2 EC_{50} (Fig. 7, *F* and *G*). These results could be explained by hypothesizing that the Arg^{393} interaction with PIP_2 couples the Ca^{2+}-induced conformational change, whereas the Lys^{392} residue interaction with PIP_2 is independent of Ca^{2+} binding. The crystal structure and docking simulation results support this idea because Lys^{392} points away from the αB helix in the absence of Ca^{2+}, whereas Arg^{393} points toward the αB helix (Fig. 1*C*, *right*). Accordingly, Ca^{2+} binding induces a helical conformational turn of αB to facilitate the Arg^{393} interaction with PIP_2 (nearly a 90° turn) but has no effect on the Lys^{392} orientation.

Hydrophobic Coupling of the αA and αB Helices Plays a Critical Role in the Activation of Slo1 Channels—How could changes in the conformation of the KDRDD loop be communicated to the PIP_2-interacting residues in the αB helix? Comparison of the 3MT5 (Asp^{367}/Glu^{535} pointing away from each other; Fig. 1*C*, *left*) and 3NAF (Asp^{367}/Glu^{535} pointing toward each other; Fig. 1*C*, *right*) structures reveals that in the 3MT5 structure, several residues between the αA and αB helices (αA, Val^{356}, Leu^{360}, Lys^{361}, and Leu^{364}; αB, Phe^{391} and Phe^{395}) form predominantly hydrophobic interactions (Figs. 1*C* and 8, *top*, *right inset*). Mutants of these residues were tested for their involvement in (*a*) the $[Ca^{2+}]_i$-induced shift in $V_{1/2}$ and (*b*) the effect on channel activation in the absence of $[Ca^{2+}]_i$. Whereas the V356A mutant showed no significant changes on either of the two effects (Fig. 8, *A*,

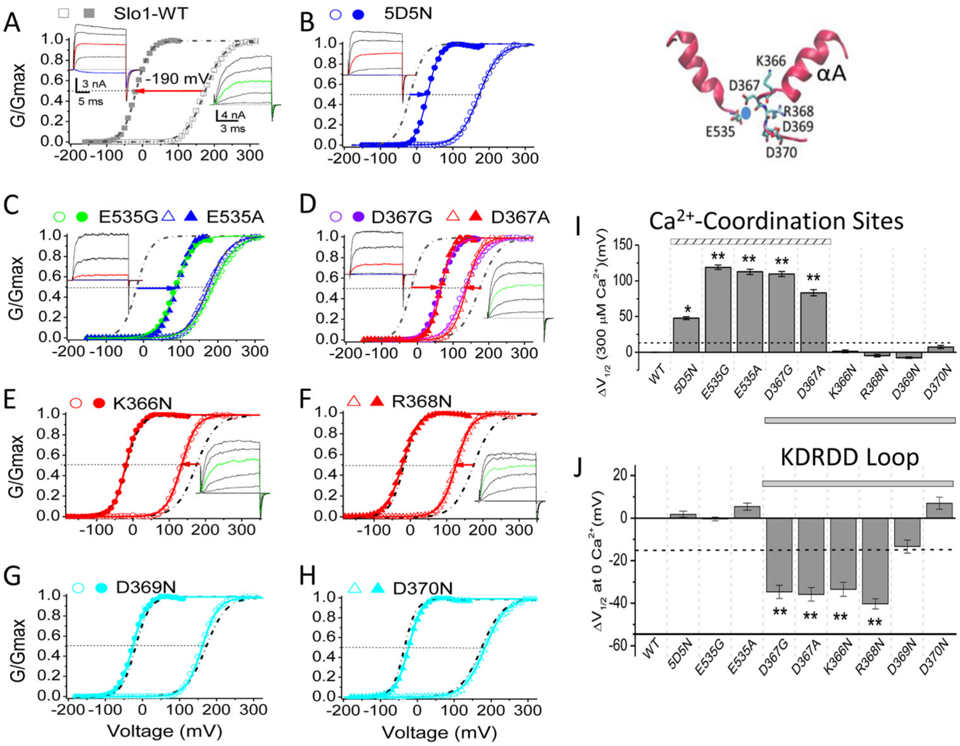

FIGURE 6. **Asp^{367} and its flanking two basic residues exert an inhibitory effect on activation of Slo1 channels in the absence of [Ca^{2+}]$_i$.** The *inset* at the *top right* shows the Ca^{2+} coordination site by the RCK1 Asp^{367} residue (in the KDRDD loop) and the Glu^{535} residue (between αH and βG) from a crystal structure (PDB code 3NAF), where the protein is shown in *ribbon form*, and the notable residues are displayed in *stick mode* and *colored* by atom type. The Ca^{2+} ion is shown in *blue*. *A–H*, normalized G-V curves for WT (*A*) and mutants (*B–H*) in 0 (*open symbols*) and 300 μM (*filled symbols*) [Ca^{2+}]$_i$. In the presence of 300 μM [Ca^{2+}]$_i$, the current traces for the G-V curves were obtained from voltage pulses with a 10-mV increment from −180 to +180 mV; the holding and repolarizing voltages were −120 mV. In the absence of [Ca^{2+}]$_i$, voltage was stepped from −100 to +300 mV, and the holding and repolarizing current was at −100 mV. For clarity, the currents shown in the *insets* are the traces elicited at −20, +40, +80, +120, and +160 mV in 300 μM [Ca^{2+}]$_i$ or at 120, 160, 200, 240, and 280 mV in 0 [Ca^{2+}]$_i$. For easy comparison, the *red-colored traces* in the *left set* highlight the currents activated at +80 mV in 300 μM [Ca^{2+}]$_i$, and the *cyan traces* highlight the currents activated at −20 mV (near the $V_{1/2}$ for Slo1-WT at 300 μM [Ca^{2+}]$_i$). The *green-colored traces* in the *right set* highlight the currents elicited at +200 mV. The *solid lines* are fits to the Boltzmann equation (see "Experimental Procedures"). For comparison, the G-V fitted curves from the Slo1 WT channel in *A* are also shown in *dashed/dotted black lines* in *B–H*. *I*, effect of mutations on Ca^{2+} sensitivity. $\Delta V_{1/2}$ (at 300 μM Ca^{2+}) = $V_{1/2(\mathrm{mut})} - V_{1/2(\mathrm{WT})}$ at 300 μM [Ca^{2+}]$_i$, where $V_{1/2}$ is the voltage where the conductance (*G*) is half-maximal. Data points represent 5–15 determinations. *J*, effect of mutations on Ca^{2+}-independent activation of Slo1 channels. $\Delta V_{1/2}$ at 0 [Ca^{2+}]$_i$ = $V_{1/2(\mathrm{mut})} - V_{1/2(\mathrm{WT})}$ at 0 μM [Ca^{2+}]$_i$. Data points represent 5–15 determinations. The *dashed horizontal bars* in *I* and *J* indicate a threshold level ($\Delta V_{1/2}$ = 15 mV) under which changes were not considered significant. *, $p < 0.01$; **, $p < 0.005$. *Error bars* indicate mean ± S.E.

G, and *H*), the L360A mutant significantly affected only the Ca^{2+}-induced shift in $V_{1/2}$ (Fig. 8, *B*, *G*, and *H*). In contrast, the K361N significantly left-shifted only the channel's activation in the absence of [Ca^{2+}]$_i$ (Fig. 8, *C*, *G*, and *H*). Ala mutations of the remaining three hydrophobic residues, Leu^{364}, Phe^{391}, and Phe^{395}, all significantly affected both effects (Fig. 8, *D–H*). Interestingly, F395A, unlike the other mutants, exhibited a greater inhibition on the channel's activation in the absence of [Ca^{2+}]$_i$ (Fig. 8, *F* and *H*). Thus, mutation of hydrophobic residues whose side chains point toward the crevice between αA and αB enabled the Ca^{2+}-dependent effect.

Mutants of all four residues that significantly altered Slo1 activation in the absence of Ca^{2+} (αA, K361N and L364A; αB, F391A and F395A) also enhanced the apparent affinity for PIP$_2$ (Fig. 9, *A–F*). The enhancement of the PIP$_2$ apparent affinity was smallest for F395A (Fig. 9, *D–F*). This residue was the only one that stood out from the otherwise perfect correlation between inhibitory effects of residues on the channel's activation in the absence of Ca^{2+} and their inhibitory effects on PIP$_2$ apparent affinity. Examination of our modeled structure of the full-length Slo1 channel that incorporated the 3NAF (Ca^{2+}-free) crystal structure suggests that Phe^{395} may come in close proximity to the Tyr^{336} residue in the C-linker that immediately follows the S6 helix (Fig. 1*C*). Thus, it is possible that the F395A mutation affected the stability of the channel's open state in a manner that extended beyond its effect on PIP$_2$ sensitivity. These results revealed that mostly hydrophobic interactions between the αA and αB helices decreased PIP$_2$ affinity, suggesting that the coupling between the KDRDD loop and the PIP$_2$ interaction residues is mediated through specific interactions in these two helices.

Mutants with Decreased Apparent Affinity to PIP$_2$ Exhibit Increased Current Rundown—Membrane patch excision of channels in ATP-free solutions frequently results in current rundown that can be reversed by application of PIP$_2$ (*e.g.* (49). However, for channels with high affinity for PIP$_2$, current rundown can be minimal or none. Slo1 excised inside-out patches in 100 μM [Ca^{2+}]$_i$ display minimal current rundown (see single channel data shown in Fig. 3), probably due to their high affinity for PIP$_2$ (apparent affinity for diC8-PIP$_2$ is ~6 μM; see Fig. 4*G*). In contrast, the K392N and R393N mutants that decreased the channel's apparent affinity for PIP$_2$ ~6–7-fold caused significant current rundown (Fig. 10, *A–H*), whereas channel activation and deactivation rates were significantly slowed down (data not shown).

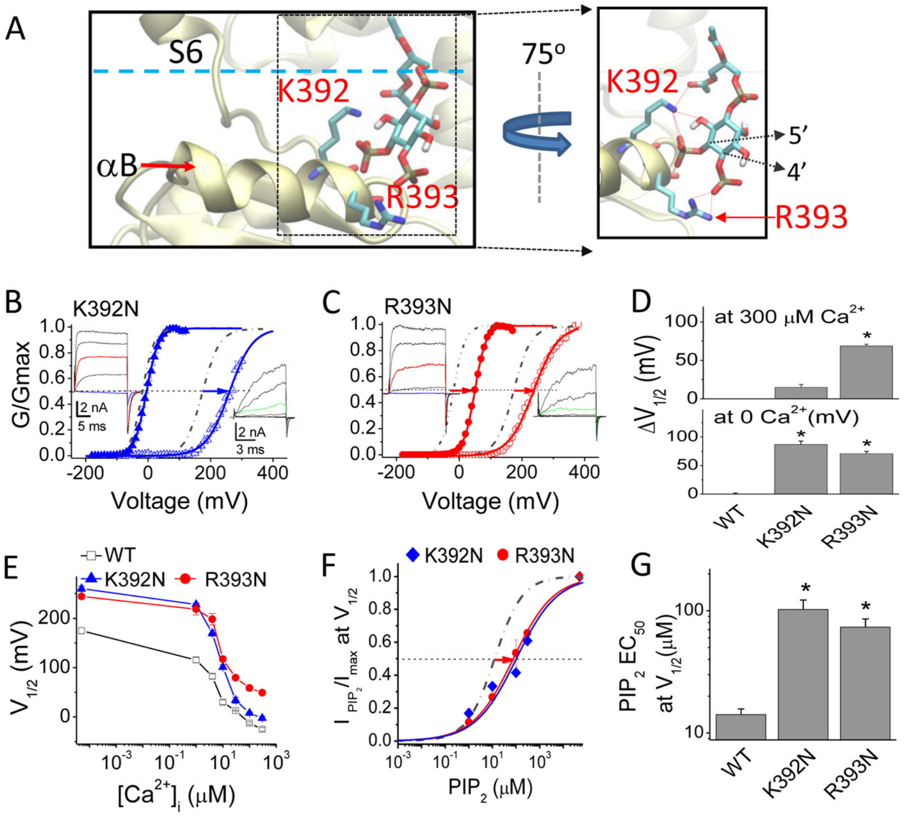

FIGURE 7. **Slo1 residues that interact with PIP_2 and affect channel activation.** *A*, docking of PIP_2 to the Slo1 cytosolic domain (PDB code 3NAF) revealed a direct interaction of PIP_2 with Lys^{392}/Arg^{393} residues in the αB helix. *B* and *C*, normalized G-V relations for K392N (*B*) and R393N (*C*) in 0 μM (*open symbols*) and 300 μM (*filled symbols*) $[Ca^{2+}]_i$. For clarity, the currents shown in the *inset* are the traces elicited at −20, +40, +80, +120, and +160 mV in 300 μM $[Ca^{2+}]_i$ (the voltages before and after the steps are −120 mV) or at 120, 160, 200, 240, and 280 mV in 0 $[Ca^{2+}]_i$) (the voltages before and after the steps were −100 mV). For easy comparison, the *red-colored traces* in the *left set* highlight the currents activated at +80 mV in 300 μM $[Ca^{2+}]_i$, and the *cyan traces* highlight the currents activated at −20 mV (near the $V_{1/2}$ for Slo1-WT at 300 μM $[Ca^{2+}]_i$). The *green traces* in the *right set* highlight the currents elicited at +200 mV. The voltage protocol for G-V curves is described under "Experimental Procedures." *Solid lines*, fits to the Boltzmann equation. *D*, the shift in $V_{1/2}$ from the G-V relationships at 300 μM (*top*) and 0 μM $[Ca^{2+}]_i$ (*bottom*) for the K392N and R393N mutants relative to the WT. $\Delta V_{1/2}$ is defined as in Fig. 6, *I* (300 μM $[Ca^{2+}]_i$) and *J* (0 μM $[Ca^{2+}]_i$). *E*, $V_{1/2}$ of G-V curves *versus* $[Ca^{2+}]_i$ for WT, K392N, and R393N mutant channels (note the similar steepness between WT and R393N). *F*, PIP_2 dose response for K392N and R393N channels in the absence of $[Ca^{2+}]_i$. Relative currents (I_{PIP2}/I_{max}) at $V_{1/2}$ were obtained in response to PIP_2 application subsequent to endogenous PIP_2 depletion (by PIP_2 Ab (1–2:1000) and poly-K^+ (300 mg/ml)) at +240 mV, near the $V_{1/2}$ for both mutations. *Solid curves* are fits to the Hill equation. Note that the maximum values were obtained from fits to the Hill equation. Data points represent 3–5 determinations. For comparison, the fitted results for WT (obtained at $V_{1/2}$ of ∼170 mV) are shown in *dashed/dotted lines*. *G*, PIP_2 EC_{50} values at $V_{1/2}$ obtained from the Hill fits from *F* ($n = 3–5$) for the two mutant channels are plotted and compared with the WT. *, $p < 0.01$. *Error bars* indicate mean ± S.E.

DISCUSSION

In this study, we examined the molecular determinants of the coupled relationship between Ca^{2+} and PIP_2 in enhancing Slo1 activity. We found that Ca^{2+} relieved a KDRDD loop inhibitory influence on channel activation by increasing the apparent affinity to PIP_2. Neutralization mutations of three KDRDD loop residues, Lys^{366}, Asp^{367}, or Arg^{368}, also relieved this inhibition in the absence of Ca^{2+} by enhancing the channel's apparent affinity to PIP_2. But where did PIP_2 act on the channel, and how did the KDRDD communicate with PIP_2? Docking simulations of PIP_2 with models of mouse Slo1 channels (based on crystal structures of the human Slo1 cytosolic domain and the rat Kv1.2/2.1 chimera transmembrane domain) identified Lys^{392} and Arg^{393} in the αB helix as putative PIP_2-interacting residues. Neutralization mutations of these two residues decreased PIP_2 sensitivity and also the channel activation in the absence of Ca^{2+}. Interestingly, Arg^{393}, which points toward the αA helix, also decreased channel activation in the presence of 300 μM Ca^{2+}, whereas Lys^{392}, which points toward the membrane, did not (Fig. 7). This result prompted us further to examine residues that enabled communication between the αA and αB helices. The two available structures of the cytosolic domains reveal a large conformational change in the structural element of αA-KDRDD-αB from the RCK2 Ca^{2+}-occupied site (3MT5) to the RCK1 site that could potentially be occupied by Ca^{2+} (3NAF). Mutation of four residues, two from the αA helix (K361N and L364A) and two from the αB helix (F391A and F395A), all affected channel activation in the absence of Ca^{2+} with a concomitant effect on the apparent affinity to PIP_2. With the exception of F395A, all other mutants decreased channel activation in the absence of Ca^{2+} (Fig. 8*H*). Phe^{395} seems to come close to Tyr^{336} (located immediately following the S6 gate), a potential interaction that may influence the response beyond the effects of this residue in its communication with the αA helix. The Hill slopes of the PIP_2 dose-response curves were typically less than 1. For Kir channels, the Hill slopes are around 1–2, suggesting that at least 1–2 PIP_2 molecules are required for channel opening. Values less than 1 could signify negative cooperativity among subunits for channel opening. Alternatively, they may signify more than one PIP_2 interaction site with

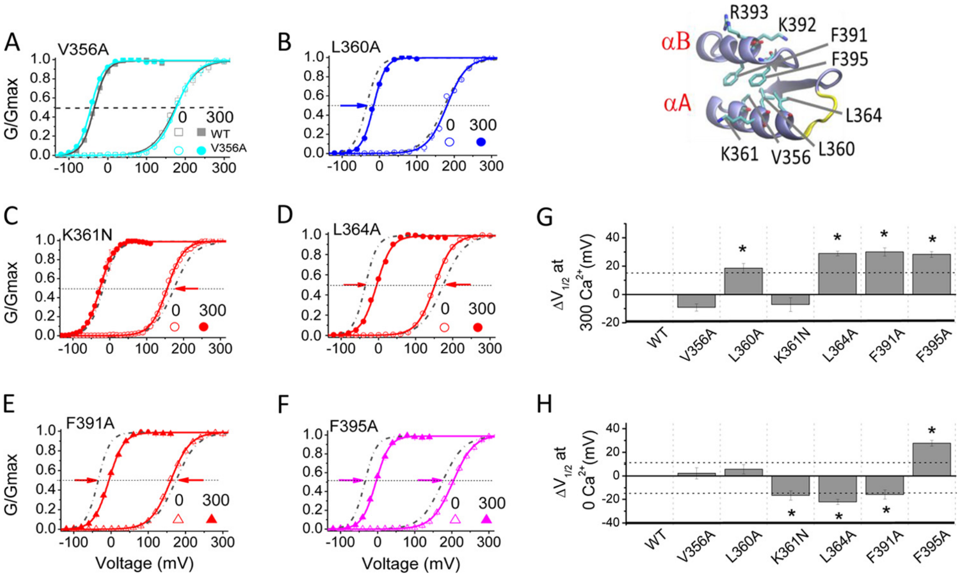

FIGURE 8. **Residues involved in the hydrophobic coupling between the αA and αB helices of the RCK1 domain affect Slo1 channel activation in the absence and presence of Ca^{2+}.** The *inset* at the *top right* shows amino acids that appear to be involved in the hydrophobic coupling between the αA and αB helices (PDB code 3MT5). The protein is shown in *ribbon form*, and the notable residues are displayed in *stick mode* and *colored* by atom type. *A–F*, normalized G-V relations for WT (*gray*) and the indicated mutants in 0 μM $[Ca^{2+}]_i$ (*open symbols*) and 300 μM $[Ca^{2+}]_i$ (*filled symbols*). The current traces to construct the G-V curves were obtained by voltage pulses from −180 to +180 mV in +20-mV increments in the presence of 300 μM $[Ca^{2+}]_i$ or from −100 to +300 mV in the absence of $[Ca^{2+}]_i$. The voltages before and after pulses were −120 mV in 300 μM $[Ca^{2+}]_i$ or −100 mV in 0 $[Ca^{2+}]_i$. Note that the data in this figure were obtained in a different batch of experiments with a different set of Ca^{2+} solutions; thus, the final Ca^{2+} concentrations are slightly different from those shown in Fig. 5. The *solid lines* are fits to the Boltzmann equation. Data points represent 4–13 determinations. *G*, effect of mutations on Ca^{2+} sensitivity. $\Delta V_{1/2}$ (at 300 μM Ca^{2+}) is defined as in the legend to Fig. 6*I*. *H*, effect of mutations on Ca^{2+}-independent activation of Slo1 channels. $\Delta V_{1/2}$ (at 0 μM Ca^{2+}) is defined as in the legend to Fig. 6*J*. *, $p < 0.05$. *Error bars* indicate mean ± S.E.

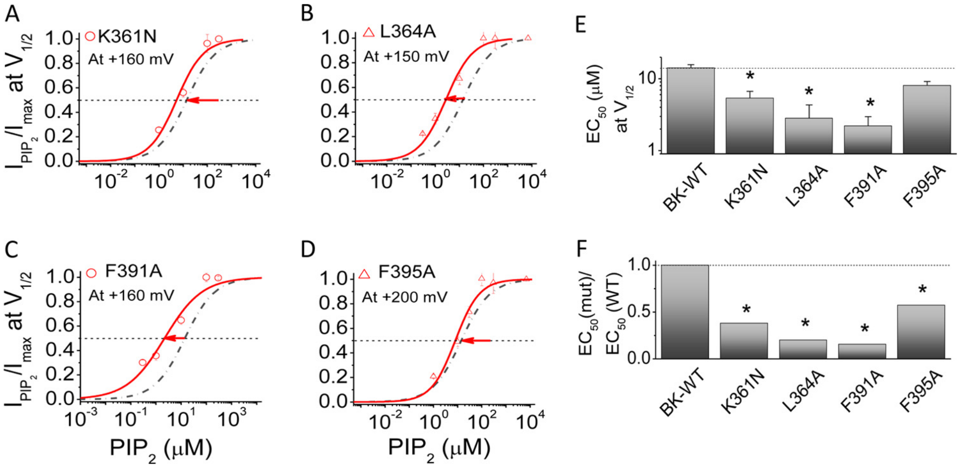

FIGURE 9. **Residues involved in the coupling between the RCK1 αA (Lys^{361} and Leu^{364}) and αB (Phe^{391} and Phe^{395}) helices alter the PIP_2 sensitivity of the channel.** *A–D*, PIP_2 dose response for mutants that changed the allosteric coupling of channel gating in the absence of $[Ca^{2+}]_i$ (*red symbols*). Relative currents (I_{PIP2}/I_{max}) at $V_{1/2}$ were obtained in response to PIP_2 application subsequent to the endogenous PIP_2 depletion (PIP_2 Ab, 1–2:1000; poly-K^+, 300 mg/ml). *Solid curves*, fits to the Hill equation with PIP_2 EC_{50} summarized in *E*. Slo1-WT is shown in the *dashed/dotted line* for comparison. Data points represent 3–6 determinations. *E*, EC_{50} at $V_{1/2}$ obtained by the Hill fits from *A–D*. *F*, -fold change in PIP_2 sensitivity of the indicated mutants relative to the WT. *, $p < 0.01$. *Error bars* indicate mean ± S.E.

similar affinities. The latter interpretation is consistent with our docking simulations of PIP_2 to the two available crystal structures, which suggest state-dependent interaction modes for PIP_2.

Our results have provided compelling evidence that when Ca^{2+} is bound to the Ca^{2+}-bowl and Ca^{2+} coordination at the RCK1 site is absent, the αA and αB helices are tightly coupled to exert an inhibitory effect on channel PIP_2 interactions. Ca^{2+} binding to the RCK1 site (or mutations that serve to "uncouple" the two helices) seems to relieve the RCK1-mediated decrease in PIP_2 affinity and to enhance channel activation. Consideration of the two available structures (3NAF and 3MT5) suggests that simultaneous Ca^{2+} binding to both RCK1 and RCK2 sites may not be possible. Our data suggested that ablation of either the Ca^{2+}-bowl site (5D5N mutant) or the RCK1 E535 coordination site, either of which decreases Ca^{2+} sensitivity, did not alter the RCK1 site inhibitory effect on activation of the Slo1α channel in the absence of Ca^{2+} (Fig. 6, *B*, *C*, and *J*). Only mutations in the αA-KDRDD-αB structural elements removed the inhibitory effect on channel activity and enhanced PIP_2 sensi-

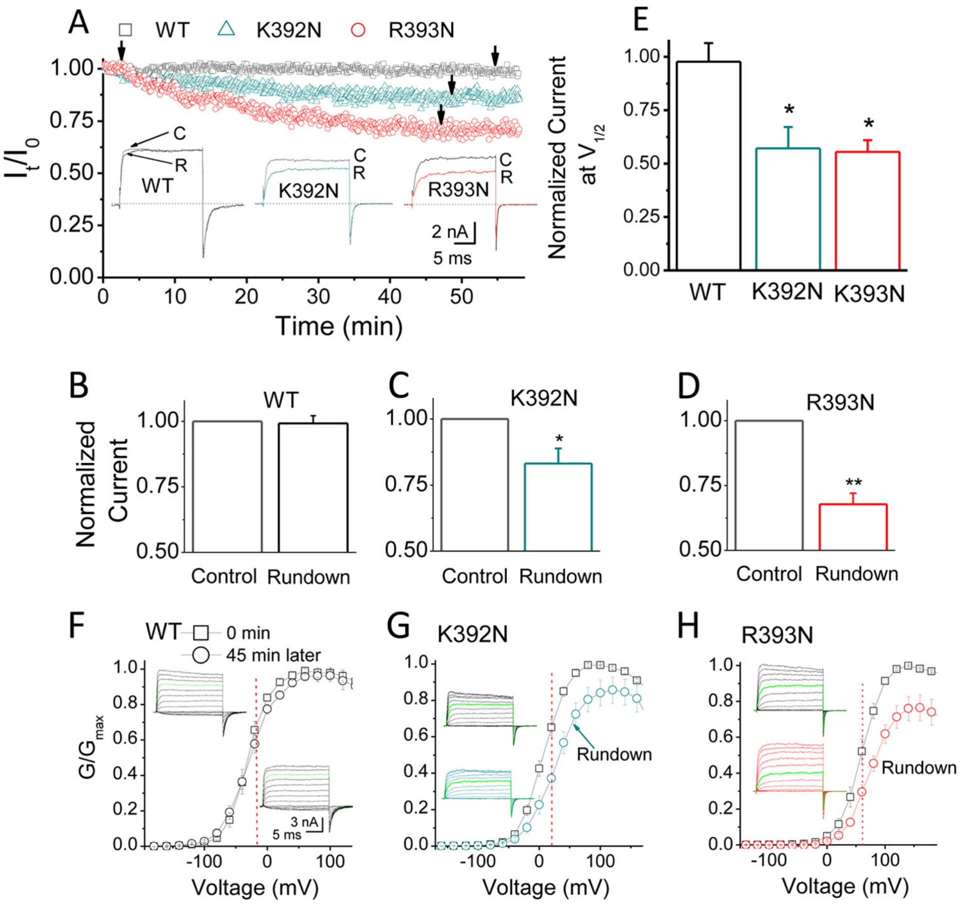

FIGURE 10. **Properties of the PIP_2-dependent rundown for the K392N and R393N mutants.** *A*, time dependence of current amplitude after patch excision. Normalized current amplitude (I_t/I_0) is plotted as a function of time in the experiment; I_0 is the current amplitude immediately following patch excision. The *insets* show the currents for WT, K392N, and R393N at the time indicated by the *arrows*. Voltage was stepped from a holding potential of −120 to +100 mV and then back to −120 mV. *C*, control; *R*, rundown. *B–D*, averaged rundown current (percentage) at +100 mV 45 min following patch excision for Slo1 WT (*B*), K392N (*C*), and R393N (*D*), as shown in *A*. *E*, averaged rundown (percentage) 45 min following patch excision comparing the K392N and R393N mutants with WT at $V_{1/2}$ (at the voltages indicated by the *red dotted lines* in *F–H*). *F–H*, normalized G-V relations of Slo1-WT (*F*), K392N (*G*), and R393N (*H*) mutants at 0 min (*black*) and 45 min (*red*) following patch excision. Recordings were performed in 100 μM $[Ca^{2+}]_i$. The *green current trace* in each of the representative traces indicates the current elicited in response to +100 mV. *, $p < 0.01$; **, $p < 0.005$. *Error bars* indicate mean ± S.E.

tivity and activation of the Slo1 channel in the absence of Ca^{2+}. These results strongly argue that it is not Ca^{2+} binding *per se* but rather the KDR residue conformations within the KDRDD loop that control channel activation in the absence of Ca^{2+} by decreasing PIP_2 sensitivity. Ca^{2+} binding to Asp^{367} serves to relieve this inhibitory effect.

The $\beta 1$ but not the $\beta 4$ accessory channel subunits have been reported to potentiate PIP_2-induced activation of BK channels (36). Using double mutant cycle analysis, the $\beta 2$ subunit was found to enhance the Ca^{2+} sensitivity of the Slo1α pore-forming subunit by directly coupling its Glu^{44} and Asp^{45} residues, located just before the first $\beta 2$ transmembrane domain, with the Lys^{392} and Arg^{393} residues of the αB helix of Slo1 (50). Because we found that Lys^{392} and Arg^{393} are critical residues for PIP_2 sensitivity, it remains to be examined whether the $\beta 2$-mediated enhancement of Slo1 currents is a reflection of altering channel-PIP_2 interactions. Similarly, whether the $\beta 1$ potentiation of PIP_2-induced activation involves the same αB residues remains to be tested.

Our study focused on the relationship of Ca^{2+} and PIP_2 sensitivity for Slo1 channel activation. We did not investigate channel residues that may also affect sensitivity to PIP_2 but are not part of the αB helix. Could such residues be specifically coupled to gating by voltage? Recent work from different laboratories, including ours, has shown that Kv1.2 channels utilize the S4-S5 linker and the N terminus to couple the movement of the voltage sensor to PIP_2 (51, 52). Thus, the relationship of PIP_2 and voltage-dependent gating in Slo1α channels remains an open question to pursue.

A recent report examining PIP_2 sensitivity of Kv channels in intact cells showed that voltage-gated channels other than Kv7 channels would not respond to a number of manipulations that decreased PIP_2 (53). However, experiments from other studies from excised patches have shown that some of the same channels are sensitive to PIP_2 (see Ref. 53 for discussion). Unlike most Kv channels tested, Kv1.2 and Shaker channels have been shown to be PIP_2-sensitive in both intact cells and excised patches (51–54). Several reasons for the differences in PIP_2 sensitivity seen between intact cells and excised patches have been considered (53), yet the relevant question is what is the physiological purpose of a high affinity interaction of a given channel with PIP_2, if it is not that PIP_2 depletion serves as a signal to inhibit channel activity? Slo1 channels are highly sensitive to PIP_2. Our studies using dose-response curves with the soluble diC8-PIP_2 following endogenous PIP_2 depletion by scavengers suggest a Slo1a EC_{50} of ~14 μM in the absence of $[Ca^{2+}]_i$ *versus* an EC_{50} of ~6 μM in 100 μM $[Ca^{2+}]_i$ (Fig. 4). The Slo3 channel has shown even higher PIP_2 sensitivity (EC_{50} ~2.5 μM) (40). As has been shown for certain channels (55), the length of the acyl chain may also contribute to the apparent affinity of Slo1 channels to PIP_2, making diC8 PIP_2 assessments of apparent affinity less meaningful (36). Regardless of what the apparent affinity of Slo1 channels is to the native PIP_2, it is clear that upon patch excision, the currents do not run down as they would for Kir channels with comparable apparent affinity for PIP_2 (*e.g.* Kir2.1 with a diC8-PIP_2 EC_{50} of ~2–3 μM). Our study has shown that the strong apparent affinity of the Slo1α channel to PIP_2 can be utilized in gating the channel by coupling the structural elements αA-KDRDD-αB and decreasing the apparent affinity of the channel for PIP_2 (EC_{50} from ~2 μM in the D367G mutant to ~14 μM in the WT).

Acknowledgments—We thank Dr. Christopher Lingle for sending cDNAs and for advice throughout this project. We thank our colleagues Drs. Leon Avery, Linda Boland, Louis De Felice, and members of the Logothetis laboratory for critical reading of the manuscript. We are grateful to Sophia Gruszecki and Heikki Vaananen for preparation of Xenopus oocytes.

REFERENCES

1. Cui, J., and Aldrich, R. W. (2000) Allosteric linkage between voltage and Ca^{2+}-dependent activation of BK-type mslo1 K^+ channels. *Biochemistry* **39,** 15612–15619
2. Horrigan, F. T., and Aldrich, R. W. (2002) Coupling between voltage sensor activation, Ca^{2+} binding and channel opening in large conductance (BK) potassium channels. *J. Gen. Physiol.* **120,** 267–305
3. Lingle, C. J. (2002) Setting the stage for molecular dissection of the regulatory components of BK channels. *J. Gen. Physiol.* **120,** 261–265
4. Shelley, C., Niu, X., Geng, Y., and Magleby, K. L. (2010) Coupling and cooperativity in voltage activation of a limited-state BK channel gating in saturating Ca^{2+}. *J. Gen. Physiol.* **135,** 461–480
5. Wei, A., Solaro, C., Lingle, C., and Salkoff, L. (1994) Calcium sensitivity of BK-type KCa channels determined by a separable domain. *Neuron* **13,** 671–681
6. Schreiber, M., and Salkoff, L. (1997) A novel calcium-sensing domain in the BK channel. *Biophys. J.* **73,** 1355–1363
7. Zhang, X., Solaro, C. R., and Lingle, C. J. (2001) Allosteric regulation of BK channel gating by Ca^{2+} and Mg^{2+} through a nonselective, low affinity divalent cation site. *J. Gen. Physiol.* **118,** 607–636
8. Bao, L., Rapin, A. M., Holmstrand, E. C., and Cox, D. H. (2002) Elimination of the BK_{Ca} channel's high-affinity Ca^{2+} sensitivity. *J. Gen. Physiol.* **120,** 173–189
9. Xia, X. M., Zhang, X., and Lingle, C. J. (2004) Ligand-dependent activation of Slo family channels is defined by interchangeable cytosolic domains. *J. Neurosci.* **24,** 5585–5591
10. Xia, X. M., Zeng, X., and Lingle, C. J. (2002) Multiple regulatory sites in large-conductance calcium-activated potassium channels. *Nature* **418,** 880–884
11. Shi, J., Krishnamoorthy, G., Yang, Y., Hu, L., Chaturvedi, N., Harilal, D., Qin, J., and Cui, J. (2002) Mechanism of magnesium activation of calcium-activated potassium channels. *Nature* **418,** 876–880
12. Bao, L., Kaldany, C., Holmstrand, E. C., and Cox, D. H. (2004) Mapping the BKCa channel's "Ca^{2+} bowl": side-chains essential for Ca^{2+} sensing. *J. Gen. Physiol.* **123,** 475–489
13. Zeng, X. H., Xia, X. M., and Lingle, C. J. (2005) Divalent cation sensitivity of BK channel activation supports the existence of three distinct binding sites. *J. Gen. Physiol.* **125,** 273–286
14. Lu, R., Alioua, A., Kumar, Y., Eghbali, M., Stefani, E., and Toro, L. (2006) MaxiK channel partners: physiological impact. *J. Physiol.* **570,** 65–72
15. Behrens, R., Nolting, A., Reimann, F., Schwarz, M., Waldschütz, R., and Pongs, O. (2000) hKCNMB3 and hKCNMB4, cloning and characterization of two members of the large-conductance calcium-activated potassium channel β subunit family. *FEBS Lett.* **474,** 99–106
16. Riazi, M. A., Brinkman-Mills, P., Johnson, A., Naylor, S. L., Minoshima, S., Shimizu, N., Baldini, A., and McDermid, H. E. (1999) Identification of a putative regulatory subunit of a calcium-activated potassium channel in the dup(3q) syndrome region and a related sequence on 22q11.2. *Genomics* **62,** 90–94
17. Du, W., Bautista, J. F., Yang, H., Diez-Sampedro, A., You, S. A., Wang, L., Kotagal, P., Lüders, H. O., Shi, J., Cui, J., Richerson, G. B., and Wang, Q. K. (2005) Calcium-sensitive potassium channelopathy in human epilepsy and paroxysmal movement disorder. *Nat. Genet.* **37,** 733–738
18. Cavalleri, G. L., Weale, M. E., Shianna, K. V., Singh, R., Lynch, J. M., Grinton, B., Szoeke, C., Murphy, K., Kinirons, P., O'Rourke, D., Ge, D., Depondt, C., Claeys, K. G., Pandolfo, M., Gumbs, C., Walley, N., McNamara, J., Mulley, J. C., Linney, K. N., Sheffield, L. J., Radtke, R. A., Tate, S. K., Chissoe, S. L., Gibson, R. A., Hosford, D., Stanton, A., Graves, T. D., Hanna, M. G., Eriksson, K., Kantanen, A. M., Kalviainen, R., O'Brien, T. J., Sander, J. W., Duncan, J. S., Scheffer, I. E., Berkovic, S. F., Wood, N. W., Doherty, C. P., Delanty, N., Sisodiya, S. M., and Goldstein, D. B. (2007) Multicentre search for genetic susceptibility loci in sporadic epilepsy syndrome and seizure types: a case-control study. *Lancet Neurol.* **6,** 970–980
19. Lorenz, S., Heils, A., Kasper, J. M., and Sander, T. (2007) Allelic association of a truncation mutation of the KCNMB3 gene with idiopathic generalized epilepsy. *Am. J. Med. Genet. B Neuropsychiatr. Genet.* **144B,** 10–13
20. Fernández-Fernández, J. M., Tomas, M., Vázquez, E., Orio, P., Latorre, R., Sentí, M., Marrugat, J., and Valverde, M. A. (2004) Gain-of-function mutation in the KCNMB1 potassium channel subunit is associated with low prevalence of diastolic hypertension. *J. Clin. Invest.* **113,** 1032–1039
21. Sentí, M., Fernández-Fernández, J. M., Tomás, M., Vázquez, E., Elosua, R., Marrugat, J., and Valverde, M. A. (2005) Protective effect of the KCNMB1 E65K genetic polymorphism against diastolic hypertension in aging women and its relevance to cardiovascular risk. *Circ. Res.* **97,** 1360–1365
22. Tomás, M., Vázquez, E., Fernández-Fernández, J. M., Subirana, I., Plata, C., Heras, M., Vila, J., Marrugat, J., Valverde, M. A., and Sentí, M. (2008) Genetic variation in the KCNMA1 potassium channel α subunit as risk factor for severe essential hypertension and myocardial infarction. *J. Hypertens.* **26,** 2147–2153
23. Nielsen, T., Burgdorf, K. S., Grarup, N., Borch-Johnsen, K., Hansen, T., Jørgensen, T., Pedersen, O., and Andersen, G. (2008) The KCNMB1 Glu65Lys polymorphism associates with reduced systolic and diastolic blood pressure in the Inter99 study of 5729 Danes. *J. Hypertens* **26,** 2142–2146
24. Kelley-Hedgepeth, A., Peter, I., Montefusco, M. C., Levy, D., Benjamin, E. J., Vasan, R. S., Mendelsohn, M. E., Housman, D., Huggins, G. S., and Mitchell, G. F. (2009) The KCNMB1 E65K variant is associated with reduced central pulse pressure in the community-based Framingham Offspring Cohort. *J. Hypertens.* **27,** 55–60
25. Soroceanu, L., Manning, T. J., Jr., and Sontheimer, H. (1999) Modulation of glioma cell migration and invasion using Cl^- and K^+ ion channel blockers. *J. Neurosci.* **19,** 5942–5954
26. Köhler, R., Degenhardt, C., Kühn, M., Runkel, N., Paul, M., and Hoyer, J. (2000) Expression and function of endothelial Ca^{2+}-activated K^+ channels in human mesenteric artery: a single-cell reverse transcriptase-polymerase chain reaction and electrophysiological study *in situ*. *Circ. Res.* **87,** 496–503
27. Liu, X., Chang, Y., Reinhart, P. H., and Sontheimer, H. (2002) Cloning and characterization of glioma BK, a novel BK channel isoform highly expressed in human glioma cells. *J. Neurosci.* **22,** 1840–1849
28. Khaitan, D., Sankpal, U. T., Weksler, B., Meister, E. A., Romero, I. A., Couraud, P. O., and Ningaraj, N. S. (2009) Role of KCNMA1 gene in breast cancer invasion and metastasis to brain. *BMC Cancer* **9,** 258
29. Seibold, M. A., Wang, B., Eng, C., Kumar, G., Beckman, K. B., Sen, S., Choudhry, S., Meade, K., Lenoir, M., Watson, H. G., Thyne, S., Williams, L. K., Kumar, R., Weiss, K. B., Grammer, L. C., Avila, P. C., Schleimer, R. P.,

Burchard, E. G., and Brenner, R. (2008) An African-specific functional polymorphism in KCNMB1 shows sex-specific association with asthma severity. *Hum. Mol. Genet.* **17,** 2681–2690

30. Lee, U. S., and Cui, J. (2010) BK channel activation: structural and functional insights. *Trends Neurosci.* **33,** 415–423
31. Zhang, G., Huang, S. Y., Yang, J., Shi, J., Yang, X., Moller, A., Zou, X., and Cui, J. (2010) Ion sensing in the RCK1 domain of BK channels. *Proc. Natl. Acad. Sci. U.S.A.* **107,** 18700–18705
32. Yuan, P., Leonetti, M. D., Pico, A. R., Hsiung, Y., and MacKinnon, R. (2010) Structure of the human BK channel Ca^{2+}-activation apparatus at 3.0 Å resolution. *Science* **329,** 182–186
33. Wu, Y., Yang, Y., Ye, S., and Jiang, Y. (2010) Structure of the gating ring from the human large-conductance Ca^{2+}-gated K^+ channel. *Nature* **466,** 393–397
34. Suh, B. C., and Hille, B. (2008) PIP2 is a necessary cofactor for ion channel function: how and why? *Annu. Rev. Biophys.* **37,** 175–195
35. Logothetis, D. E., Petrou, V. I., Adney, S. K., and Mahajan, R. (2010) Channelopathies linked to plasma membrane phosphoinositides. *Pflugers Arch.* **460,** 321–341
36. Vaithianathan, T., Bukiya, A., Liu, J., Liu, P., Asuncion-Chin, M., Fan, Z., and Dopico, A. (2008) Direct regulation of BK channels by phosphatidylinositol 4,5-bisphosphate as a novel signaling pathway. *J. Gen. Physiol.* **132,** 13–28
37. Tang, Q. Y., Zeng, X. H., and Lingle, C. J. (2009) Closed-channel block of BK potassium channels by bbTBA requires partial activation. *J. Gen. Physiol.* **134,** 409–436
38. Zhou, Y., Tang, Q. Y., Xia, X. M., and Lingle, C. J. (2010) Glycine 311, a determinant of paxilline block in BK channels: a novel bend in the BK S6 helix. *J. Gen. Physiol.* **135,** 481–494
39. Zhang, Z., Zhou, Y., Ding, J. P., Xia, X. M., and Lingle, C. J. (2006) A limited access compartment between the pore domain and cytosolic domain of the BK channel. *J. Neurosci.* **26,** 11833–11843
40. Tang, Q. Y., Zhang, Z., Xia, J., Ren, D., and Logothetis, D. E. (2010) Phosphatidylinositol 4,5-bisphosphate activates Slo3 currents and its hydrolysis underlies the epidermal growth factor-induced current inhibition. *J. Biol. Chem.* **285,** 19259–19266
41. Zhang, Z., Rosenhouse-Dantsker, A., Tang, Q. Y., Noskov, S., and Logothetis, D. E. (2010) The RCK2 domain uses a coordination site present in Kir channels to confer sodium sensitivity to Slo2.2 channels. *J. Neurosci.* **30,** 7554–7562
42. Zhang, Z., Tang, Q. Y., Alaimo, J. T., Davies, A. G., Bettinger, J. C., and Logothetis, D. E. (2013) SLO-2 isoforms with unique Ca^{2+}- and voltage-dependence characteristics confer sensitivity to hypoxia in *C. elegans*. *Channels* **7,** 194–205
43. Tang, Q. Y., Zhang, Z., Xia, X. M., and Lingle, C. J. (2010) Block of mouse Slo1 and Slo3 K^+ channels by CTX, IbTX, TEA, 4-AP and quinidine. *Channels* **4,** 22–41
44. Thompson, J. D., Higgins, D. G., and Gibson, T. J. (1994) Improved sensitivity of profile searches through the use of sequence weights and gap excision. *Comput. Appl. Biosci.* **10,** 19–29
45. Sali, A., and Blundell, T. L. (1993) Comparative protein modelling by satisfaction of spatial restraints. *J. Mol. Biol.* **234,** 779–815
46. Morris, G. M., Goodsell, D. S., Halliday, R. S., Huey, R., Hart, W. E., Belew, R. K., and Olson, A. J. (1998) Automated docking using a Lamarckian genetic algorithm and empirical binding free energy function. *J. Comput. Chem.* **19,** 1639–1662
47. Rohács, T., Lopes, C. M., Michailidis, I., and Logothetis, D. E. (2005) PI(4,5)P2 regulates the activation and desensitization of TRPM8 channels through the TRP domain. *Nat. Neurosci.* **8,** 626–634
48. Yang, J., Krishnamoorthy, G., Saxena, A., Zhang, G., Shi, J., Yang, H., Delaloye, K., Sept, D., and Cui, J. (2010) An epilepsy/dyskinesia-associated mutation enhances BK channel activation by potentiating Ca^{2+} sensing. *Neuron* **66,** 871–883
49. Zhang, H., He, C., Yan, X., Mirshahi, T., and Logothetis, D. E. (1999) Activation of inwardly rectifying K^+ channels by distinct PtdIns(4,5)P2 interactions. *Nat. Cell Biol.* **1,** 183–188
50. Hou, P., Zeng, W., Gan, G., Lv, C., Guo, X., Zhang, Z., Liu, H., Wu, Y., Yao, J., Wei, A. D., Wang, S., and Ding, J. (2013) Inter-α/β subunits coupling mediating pre-inactivation and augmented activation of BKCa(β2). *Sci. Rep.* **3,** 1666
51. Rodriguez-Menchaca, A. A., Adney, S. K., Tang, Q. Y., Meng, X. Y., Rosenhouse-Dantsker, A., Cui, M., and Logothetis, D. E. (2012) PIP2 controls voltage-sensor movement and pore opening of Kv channels through the S4-S5 linker. *Proc. Natl. Acad. Sci. U.S.A.* **109,** E2399–E2408
52. Abderemane-Ali, F., Es-Salah-Lamoureux, Z., Delemotte, L., Kasimova, M. A., Labro, A. J., Snyders, D. J., Fedida, D., Tarek, M., Baró, I., and Loussouarn, G. (2012) Dual effect of phosphatidylinositol (4,5)-bisphosphate PIP_2 on Shaker K^+ [corrected] channels. *J. Biol. Chem.* **287,** 36158–36167
53. Kruse, M., Hammond, G. R., and Hille, B. (2012) Regulation of voltage-gated potassium channels by PI(4,5)P2. *J. Gen. Physiol.* **140,** 189–205
54. Kruse, M., and Hille, B. (2013) The phosphoinositide sensitivity of the KV channel family. *Channels* **7,** 530–536
55. Rohács, T., Chen, J., Prestwich, G. D., and Logothetis, D. E. (1999) Distinct specificities of inwardly rectifying K^+ channels for phosphoinositides. *J. Biol. Chem.* **274,** 36065–36072
56. Long S. B., Tao X., Campbell E. B., MacKinnon R. (2007) Atomic structure of a voltage-dependent K^+ channel in a lipid membrane-like environment. *Nature* **450,** 376–382